

Large anomalous Nernst effect in a van der Waals ferromagnet

Fe_3GeTe_2

Jinsong Xu^{1*}, W. Adam Phelan², C.L. Chien¹

¹ Department of Physics and Astronomy, Johns Hopkins University, Baltimore, Maryland 21218, USA

² Department of Chemistry, Johns Hopkins University, Baltimore, Maryland 21218, USA

Abstract

Anomalous Nernst effect, a result of charge current driven by temperature gradient, provides a probe of the topological nature of materials due to its sensitivity to the Berry curvature near the Fermi level. Fe_3GeTe_2 , one important member of the recently discovered two-dimensional van der Waals magnetic materials, offers a unique platform for anomalous Nernst effect because of its metallic and topological nature. Here, we report the observation of large anomalous Nernst effect in Fe_3GeTe_2 . The anomalous Hall angle and anomalous Nernst angle are about 0.07 and 0.09 respectively, far larger than those in common ferromagnets. By utilizing the Mott relation, these large angles indicate a large Berry curvature near the Fermi level, consistent with the recent proposal for Fe_3GeTe_2 as a topological nodal line semimetal candidate. Our work provides evidence of Fe_3GeTe_2 as a topological ferromagnet, and demonstrates the feasibility of using two-dimensional magnetic materials and their band topology for spin caloritronics applications.

Key words: Anomalous Nernst effect, Fe_3GeTe_2 , spin caloritronics, topological ferromagnet

*email: jxu94@jhu.edu

The recently discovered two-dimensional (2D) van der Waals (vdW) magnets [1-8], providing new constituent materials for spintronics and caloritronics, have attracted much attention. To date, most 2D vdW ferromagnets are semiconductors (e.g., $\text{Cr}_2\text{Ge}_2\text{Te}_6$) and insulators (e.g., CrI_3), with Fe_3GeTe_2 (FGT) being the only ferromagnetic (FM) metal. Electrical switching of FGT by spin orbit torque [9,10] and tunneling magnetoresistance in FGT/h-BN/FGT heterostructure [11] have recently been demonstrated. FGT also has the highest Curie temperature (T_c) among the 2D vdW ferromagnets, and the value of T_c in thin FGT films can be tuned by ionic gating up to about room temperature [3]. Furthermore, the topological nature of FGT gives rise to some intriguing phenomena, for example, the observation of large anomalous Hall effect (AHE) [12] and magnetic skyrmions [13-15]. Of particular interest is the anomalous Nernst effect (ANE) in topological materials because the special band topology in these materials could introduce a very large ANE [16-19], which shares some similarities with, but also differences from, the better known AHE. In AHE and ANE, the current is driven by an electric field and temperature gradient ∇T respectively, while a voltage is measured perpendicular to both the current and the magnetization \mathbf{M} of the material. While the AHE is dominated by the sum of the Berry curvatures for all the occupied states, ANE is determined by the Berry curvature at the Fermi level ϵ_F , thus providing a different probe of the Berry curvature near ϵ_F and the topological nature of materials [16-19]. Therefore, FGT provides a unique platform for studying the ANE in 2D vdW ferromagnets and their topological properties.

In this work, we report the observation of AHE and ANE in exfoliated FGT thin film devices. We have determined σ_{xx} (defined as $\frac{\rho_{xx}}{\rho_{xx}^2 + \rho_{xy}^2}$), and σ_{xy} ($-\frac{\rho_{xy}}{\rho_{xx}^2 + \rho_{xy}^2}$), the longitudinal and the transverse (or Hall) conductivities respectively, as well as S_{xx} ($-\nabla V_x / \nabla T_x$) and S_{yx} ($-\nabla V_y / \nabla T_x$), the longitudinal and the transverse Seebeck coefficients respectively. We have found very large AHE angle ($\theta_H = \sigma_{xy} / \sigma_{xx}$) and very large ANE angle ($\theta_N = S_{yx} / S_{xx}$), about 0.07 and 0.09 at low temperatures respectively, much larger than those found in common FM metals of 0.02 or less [12,20-23]. This places FGT outside the realm of common FM materials. We further found that the temperature dependence of the transverse thermoelectric conductivity α_{xy} follows the Mott relation $\alpha_{xy} = -(\frac{\pi^2 k_B^2}{3e})T(\frac{\partial \sigma_{xy}}{\partial \epsilon})_{\epsilon_F}$, and the Hall resistivity follows the scaling relation of $\rho_{xy} = \lambda M \rho_{xx}^n$ with $n \approx 2$, where λ represents the strength of the spin-orbit coupling, M the magnetization, and ρ_{xx} (ρ_{xy}) the longitudinal (transverse) resistivity. This scaling relationship together with the observed large anomalous Hall conductivity ($360 \sim 400 \Omega^{-1} \text{cm}^{-1}$) indicates the origin of the observed large AHE and ANE in FGT is primarily the intrinsic mechanism from the large Berry curvature, and not scattering, such as skew scattering and side-jump [23-25], consistent with the topological nature of FGT [12,26]. Our work provides evidence for FGT as a topological ferromagnetic metal, and demonstrates the feasibility of using 2D vdW magnetic materials and their band topology for spin caloritronic applications.

The vdW material of Fe_3GeTe_2 consists of Fe_3Ge slabs sandwiched by two layers of Te atoms and a van der Waals gap between the adjacent Te layers as shown in Fig. 1a. Single crystals of bulk FGT, grown by chemical vapor transport method, exhibit a lattice

constant of $c = 16.36 \text{ \AA}$, measured by X-ray diffraction (for details, see Supporting Information). The magnetic properties of bulk FGT, characterized by a superconducting quantum interference device, show a saturation magnetization of about 310 emu cm^{-3} with a magnetic moment of $1.25 \mu_B$ per Fe atom, and Curie temperature of about 200 K (see Supporting Information Fig. S3). Thin FGT flake is mechanically exfoliated onto heavily n -doped Si wafer with a 300 nm SiO_2 layer, then transferred onto pre-patterned Au contacts using dry transferred method (see Supporting Information for details). The thickness of our FGT samples are about 20~40 nm. Fig. 1b shows the schematic of a finished FGT device. There are two Au electrodes on the Si/ SiO_2 substrate used as heaters to generate a lateral temperature gradient ∇T_x and also as a thermometer to measure the local temperature (see Supporting Information). There is a ~20 nm h-BN insulating layer to electrically isolate the Au heaters and the FGT layer. On top of h-BN, there are Au electrodes to make electrical contact to the FGT layer to measure the longitudinal voltage V_x and transverse voltage V_y . For the measurements of both AHE and ANE, the magnetic field is applied out-of-plane, along the z -axis, unless otherwise noted.

We first examine the magnetic properties of FGT through the anomalous Hall effect with magnetometry results in the Supporting Information. For AHE, a small DC current (1 μA) is applied along the x -axis in FGT while both longitudinal voltage V_x and transverse voltage V_y are measured. We experimentally measured the longitudinal (ρ_{xx}) and the transverse (ρ_{xy}) resistivities, which convert to $\sigma_{xx} = \frac{\rho_{xx}}{\rho_{xx}^2 + \rho_{xy}^2}$ and $\sigma_{xy} = -\frac{\rho_{xy}}{\rho_{xx}^2 + \rho_{xy}^2}$, the longitudinal and the transverse (or Hall) conductivities respectively for quasi 2D materials. As shown in Fig. 2a, at low temperatures (50 K), the Hall conductivity σ_{xy}

shows a rectangular hysteresis loop with sharp switching under an external magnetic field H_z , suggesting a single magnetic domain over the entire device. Together with the near 100% remnant σ_{xy} at zero field, these ferromagnetic hallmarks indicate thin FGT device exhibits strong perpendicular magnetic anisotropy (PMA) with the magnetic moments pointing in the out-of-plane direction. Thin films of common ferromagnets, hampered by the large shape anisotropy of $4\pi M$, rarely achieve PMA without very strong crystalline anisotropy or broken inversion symmetry and interface charge transfer. As the temperature increases (e.g., 140 K in Fig. 2a), the rectangular hysteresis loop gradually evolves into narrow-waist shape due to the weakened PMA and the formation of labyrinthine domain structure [4]. The temperature dependence of the Hall conductivity σ_{xy} extrapolated to 0 Oe and the longitudinal conductivity σ_{xx} is shown in Fig. 2b. For increasing temperature, the value of σ_{xy} decreases, and vanishes around 200 K, similar to bulk single crystals of FGT. The longitudinal conductivity σ_{xx} varies about 10% within the measured temperature range. Very significantly, the Hall angle $\theta_H = \sigma_{xy}/\sigma_{xx}$ reaches about 0.07 at low temperatures, similar to previous reports [12], much higher than those of common ferromagnets (≤ 0.02) [20-23].

We next describe the anomalous Nernst effect results in thin FGT devices. As depicted in Fig. 1b, by applying a DC current 14 mA to the right side heater, we generate an in-plane temperature gradient ∇T_x of about $1.3 \text{ K } \mu\text{m}^{-1}$. The transverse voltage V_y is measured as a function of external perpendicular magnetic field H_z as shown in Fig. 3a. Similar to that of AHE, we observe a rectangular hysteretic ANE loop. When we apply 12 mA current to the left side heater to generate an opposite temperature gradient ∇T_x of about $-1.1 \text{ K } \mu\text{m}^{-1}$, we observe a similar but reversed rectangular hysteresis loop as shown

in Fig. 3b. These results conclusively demonstrate ANE in the FGT device, after we address one experimental issue. It is well known that for thin films on thick substrates, the intended in-plane temperature gradient (∇T_x) is often accompanied inadvertently by an out-of-plane temperature gradient (∇T_z) due to the thermal conduction through the much thicker substrate. The latter may contribute an ANE voltage via $\nabla T_z \times M_x$, e.g., in permalloy thin films on Si substrate, where permalloy has in-plane magnetization M_x [20]. To assess and eliminate this possible contribution, we apply a large magnetic field H_x up to 6 kOe along the x direction and observed no appreciable signal (see Supporting Information Fig. S5). This is because of the PMA of FGT is so strong that there is no measurable M_x even with the presence of a large in-plane magnetic field. Thus all the measured thermal voltage is due to the anomalous Nernst signal of $\nabla T_x \times M_z$ in FGT.

To gain further insight and extract the Seebeck coefficients at zero field, provided by the robust PMA, we measure the ANE in the FGT devices at different temperatures T^* , and also with different temperature gradients ∇T_x , as summarized in Fig. 3c and 3d. The longitudinal voltage V_x and the transverse voltage V_y are displayed in colors as a function of T^* and ∇T_x . Using the definitions of $S_{xx} = -\nabla V_x / \nabla T_x$ and $S_{yx} = -\nabla V_y / \nabla T_x$, we obtain the ANE angle $\theta_N = S_{yx} / S_{xx}$ via LV_y / WV_x , where $L = 10 \mu\text{m}$ and $W = 5 \mu\text{m}$ are the length and width of the sample respectively. We obtained very large ANE angle θ_N of as much as 0.09 at low temperature, a value much higher than those of common ferromagnets (<0.02) [20,21]. These large ANE angle θ_N of 0.09 corroborates with the similarly large AHE angle θ_H of 0.07, both are much larger than those in common FM metals of ≤ 0.02 .

With the measured longitudinal (S_{xx}) and transverse (S_{yx}) Seebeck coefficients, we can obtain the transverse thermoelectric conductivity $-\alpha_{xy}$. The temperature dependence of the transverse and longitudinal Seebeck coefficient S_{yx} and S_{xx} is shown in Fig. 4a. The laws of thermodynamics and FM ordering dictate the temperature dependence of S_{yx} , which must vanish at $T = 0$ K, remains finite below T_C and becomes negligible above T_C . With the aid of the Mott relation [16,23,27], quantitative analysis can be performed. The transverse thermoelectric conductivity $-\alpha_{xy}$ and Seebeck coefficients are related through

$$\alpha_{xy} = \sigma_{xx}S_{xy} + \sigma_{xy}S_{xx} = -\sigma_{xx}S_{yx} + \sigma_{xy}S_{xx}, \quad (1)$$

Therefore, α_{xy} can be determined from the measured σ_{xx} , σ_{xy} , S_{xx} and S_{yx} . On the other hand, if the Mott relation holds, α_{xy} can be obtained from via $\alpha_{xy} = -(\frac{\pi^2 k_B^2}{3e})T(\frac{\partial \sigma_{xy}}{\partial \epsilon})_{\epsilon_F}$, and S_{xx} from $S_{xx} = -(\frac{\pi^2 k_B^2}{3e})T(\frac{\partial \ln \sigma_{xx}}{\partial \epsilon})_{\epsilon_F}$, where k_B is the Boltzmann constant, ϵ is the energy, and ϵ_F is the Fermi energy. By substituting the scaling relationship for the Hall resistivity $\rho_{xy} = \lambda M \rho_{xx}^n$ into the Mott relation and Eq. (1), we have [20,28]

$$S_{yx} = \sigma_{xy}/\sigma_{xx} \left(\left(\frac{\pi^2 k_B^2}{3e} \right) \frac{(\frac{\partial \lambda}{\partial \epsilon})_{\epsilon_F}}{\lambda} T + (n-1)S_{xx} \right), \quad (2)$$

$$\alpha_{xy} = -\sigma_{xy} \left(\left(\frac{\pi^2 k_B^2}{3e} \right) \frac{(\frac{\partial \lambda}{\partial \epsilon})_{\epsilon_F}}{\lambda} T + (n-2)S_{xx} \right). \quad (3)$$

To examine the Mott relation and determine the exponent n , we use Eq. (2) and Eq. (3) to fit S_{yx} and α_{xy} to search for the best-fit values of $(\frac{\partial \lambda}{\partial \epsilon})_{\epsilon_F}/\lambda$ and n , as shown in Fig. 4. The best-fit exponent is $n = 2.3 \pm 0.1$ (blue solid curves). The exponent is clearly close to $n = 2$, and not $n = 1$, as shown in Fig. 4. The scaling relationship with $n = 2$ indicates that

the intrinsic mechanism or side-jump, instead of skew scattering, dominates AHE and ANE [23-25] in FGT. Previous reports have shown the intrinsic mechanism dominates AHE in FGT [12,26], therefore n close to 2 favors intrinsic mechanism in FGT. At the same time, the anomalous Hall conductivity is $\sigma_{xy} \approx 360 \sim 400 \text{ } \Omega^{-1} \text{ cm}^{-1}$ at low temperature, which is close to the intrinsic contribution $\sigma_{xy,in} \approx e^2/ha_z \approx 470 \text{ } \Omega^{-1} \text{ cm}^{-1}$, where h is Planck constant and a_z is the interlayer distance ($a_z = c/2 = 8.18 \text{ } \text{\AA}$). This further corroborates the intrinsic Berry curvature as the primary source of the observed large AHE angle and ANE angle. This is consistent with the recent proposal of FGT as a topological nodal line semimetal with a large Berry curvature from the nodal line [12]. This may be the reasons for the exceptionally large AHE angle θ_H and ANE angle θ_N of 0.07 and 0.09, far larger than those in common ferromagnets.

In summary, we have observed ANE in exfoliated 2D van der Waals ferromagnetic metallic Fe_3GeTe_2 thin film devices. We have observed exceptionally large anomalous Nernst effect angle θ_N of 0.09, corroborated by the similarly large anomalous Hall effect angle θ_H of 0.07, much larger than the values of ≤ 0.02 for common ferromagnetic metals. From the measured transport coefficients and the Mott relation, we find the large Berry curvature is responsible for the observed large AHE angle and ANE angle, which provides evidence for FGT as a topological ferromagnet. Our results demonstrate the feasibility of using 2D vdW magnetic materials and their band topology for spin caloritronics applications.

ASSOCIATED CONTENT

Supporting Information

A description of device fabrication, Fe₃GeTe₂ bulk crystal growth and characterization, temperature calibration, and anomalous Nernst contribution from vertical temperature gradient.

AUTHOR INFORMATION

Corresponding Author

*E-mail: jxu94@jhu.edu

Authors contributions

J.X. and C.L.C. conceived the experiment. W.A.P. synthesized the bulk crystals. J.X. performed the experiment. J.X. and C.L.C. wrote the manuscript with the input from all authors. All the authors discussed the results.

Notes

The authors declare no competing interests.

ACKNOWLEDGEMENTS

This work was supported by the National Science Foundation under grant DMREF-1729555. The bulk crystals were grown in the Platform for the Accelerated Realization, Analysis, and Discovery of Interface Materials (PARADIM) facilities supported by the National Science Foundation under Cooperative Agreement No. DMR-1539918.

REFERENCES

- 1 Huang, B., Clark, G., Navarro-Moratalla, E., Klein, D. R., Cheng, R., Seyler, K. L., Zhong, D., Schmidgall, E., McGuire, M. A., Cobden, D. H., Yao, W., Xiao, D., Jarillo-Herrero, P. & Xu, X. Layer-dependent ferromagnetism in a van der Waals crystal down to the monolayer limit. *Nature* **546**, 270 (2017).
- 2 Gong, C., Li, L., Li, Z., Ji, H., Stern, A., Xia, Y., Cao, T., Bao, W., Wang, C., Wang, Y., Qiu, Z. Q., Cava, R. J., Louie, S. G., Xia, J. & Zhang, X. Discovery of intrinsic ferromagnetism in two-dimensional van der Waals crystals. *Nature* **546**, 265 (2017).
- 3 Deng, Y., Yu, Y., Song, Y., Zhang, J., Wang, N. Z., Sun, Z., Yi, Y., Wu, Y. Z., Wu, S., Zhu, J., Wang, J., Chen, X. H. & Zhang, Y. Gate-tunable room-temperature ferromagnetism in two-dimensional Fe_3GeTe_2 . *Nature* **563**, 94 (2018).
- 4 Fei, Z., Huang, B., Malinowski, P., Wang, W., Song, T., Sanchez, J., Yao, W., Xiao, D., Zhu, X., May, A. F., Wu, W., Cobden, D. H., Chu, J.-H. & Xu, X. Two-dimensional itinerant ferromagnetism in atomically thin Fe_3GeTe_2 . *Nat. Mater.* **17**, 778 (2018).
- 5 O'Hara, D. J., Zhu, T., Trout, A. H., Ahmed, A. S., Luo, Y. K., Lee, C. H., Brenner, M. R., Rajan, S., Gupta, J. A., McComb, D. W. & Kawakami, R. K. Room temperature intrinsic ferromagnetism in epitaxial manganese selenide films in the monolayer limit. *Nano Lett.* **18**, 3125 (2018).
- 6 Bonilla, M., Kolekar, S., Ma, Y., Diaz, H. C., Kalappattil, V., Das, R., Eggers, T., Gutierrez, H. R., Phan, M.-H. & Batzill, M. Strong room-temperature ferromagnetism in VSe_2 monolayers on van der Waals substrates. *Nat. Nanotechnol.* **13**, 289 (2018).
- 7 Gibertini, M., Koperski, M., Morpurgo, A. F. & Novoselov, K. S. Magnetic 2D materials and heterostructures. *Nat. Nanotechnol.* **14**, 408 (2019).
- 8 Gong, C. & Zhang, X. Two-dimensional magnetic crystals and emergent heterostructure devices. *Science* **363**, 706 (2019).
- 9 Alghamdi, M., Lohmann, M., Li, J., Jothi, P. R., Shao, Q., Aldosary, M., Su, T., Fokwa, B. P. T. & Shi, J. Highly efficient spin-orbit torque and switching of layered ferromagnet Fe_3GeTe_2 . *Nano Lett.* **19**, 4400 (2019).
- 10 Wang, X., Tang, J., Xia, X., He, C., Zhang, J., Liu, Y., Wan, C., Fang, C., Guo, C., Yang, W., Guang, Y., Zhang, X., Xu, H., Wei, J., Liao, M., Lu, X., Feng, J., Li, X., Peng, Y., Wei, H., Yang, R., Shi, D., Zhang, X., Han, Z., Zhang, Z., Zhang, G., Yu, G. & Han, X. Current-driven magnetization switching in a van der Waals ferromagnet Fe_3GeTe_2 . *arXiv preprint arXiv:1902.05794* (2019).
- 11 Wang, Z., Sapkota, D., Taniguchi, T., Watanabe, K., Mandrus, D. & Morpurgo, A. F. Tunneling spin valves based on $\text{Fe}_3\text{GeTe}_2/\text{hBN}/\text{Fe}_3\text{GeTe}_2$ van der Waals heterostructures. *Nano Lett.* **18**, 4303 (2018).
- 12 Kim, K., Seo, J., Lee, E., Ko, K.-T., Kim, B. S., Jang, B. G., Ok, J. M., Lee, J., Jo, Y. J., Kang, W., Shim, J. H., Kim, C., Yeom, H. W., Min, B. I., Yang, B.-J. & Kim, J. S. Large anomalous Hall current induced by topological nodal lines in a ferromagnetic van der Waals semimetal. *Nat. Mater.* **17**, 794 (2018).
- 13 Park, T.-E., Peng, L., Zhang, X., Kim, S. J., Song, K. M., Kim, K., Weigand, M., Schütz, G., Finizio, S., Raabe, J., Xia, J., Zhou, Y., Ezawa, M., Liu, X., Chang, J., Koo, H. C., Kim, Y. D., Yu, X. & Woo, S. Observation of magnetic skyrmion crystals in a van der Waals ferromagnet Fe_3GeTe_2 . *arXiv preprint arXiv:1907.01425* (2019).
- 14 Wu, Y., Zhang, S., Zhang, J., Wang, W., Zhu, Y. L., Hu, J., Wong, K., Fang, C., Wan, C., Han, X., Shao, Q., Taniguchi, T., Watanabe, K., Mao, Z., Zhang, X. & Wang, K. L. Néel-type

- skyrmion in $\text{WTe}_2/\text{Fe}_3\text{GeTe}_2$ van der Waals heterostructure. *arXiv preprint arXiv:1907.11349* (2019).
- 15 Wang, H., Wang, C., Zhu, Y., Li, Z.-A., Zhang, H., Tian, H., Shi, Y., Yang, H. & Li, J. Direct observations of chiral spin textures in van der Waals magnet Fe_3GeTe_2 nanolayers. *arXiv preprint arXiv:1907.08382* (2019).
 - 16 Xiao, D., Yao, Y., Fang, Z. & Niu, Q. Berry-phase effect in anomalous thermoelectric transport. *Phys. Rev. Lett.* **97**, 026603 (2006).
 - 17 Ikhlas, M., Tomita, T., Koretsune, T., Suzuki, M.-T., Nishio-Hamane, D., Arita, R., Otani, Y. & Nakatsuji, S. Large anomalous Nernst effect at room temperature in a chiral antiferromagnet. *Nat. Phys.* **13**, 1085 (2017).
 - 18 Sakai, A., Mizuta, Y. P., Nugroho, A. A., Sihombing, R., Koretsune, T., Suzuki, M.-T., Takemori, N., Ishii, R., Nishio-Hamane, D., Arita, R., Goswami, P. & Nakatsuji, S. Giant anomalous Nernst effect and quantum-critical scaling in a ferromagnetic semimetal. *Nat. Phys.* **14**, 1119 (2018).
 - 19 Li, X., Xu, L., Ding, L., Wang, J., Shen, M., Lu, X., Zhu, Z. & Behnia, K. Anomalous Nernst and Righi-Leduc Effects in Mn_3Sn : Berry Curvature and Entropy Flow. *Phys. Rev. Lett.* **119**, 056601 (2017).
 - 20 Chuang, T. C., Su, P. L., Wu, P. H. & Huang, S. Y. Enhancement of the anomalous Nernst effect in ferromagnetic thin films. *Phys. Rev. B* **96**, 174406 (2017).
 - 21 Hasegawa, K., Mizuguchi, M., Sakuraba, Y., Kamada, T., Kojima, T., Kubota, T., Mizukami, S., Miyazaki, T. & Takanashi, K. Material dependence of anomalous Nernst effect in perpendicularly magnetized ordered-alloy thin films. *Appl. Phys. Lett.* **106**, 252405 (2015).
 - 22 Miyasato, T., Abe, N., Fujii, T., Asamitsu, A., Onoda, S., Onose, Y., Nagaosa, N. & Tokura, Y. Crossover behavior of the anomalous Hall effect and anomalous Nernst effect in itinerant ferromagnets. *Phys. Rev. Lett.* **99**, 086602 (2007).
 - 23 Onoda, S., Sugimoto, N. & Nagaosa, N. Quantum transport theory of anomalous electric, thermoelectric, and thermal Hall effects in ferromagnets. *Phys. Rev. B* **77**, 165103 (2008).
 - 24 Onoda, S., Sugimoto, N. & Nagaosa, N. Intrinsic versus extrinsic anomalous Hall effect in ferromagnets. *Phys. Rev. Lett.* **97**, 126602 (2006).
 - 25 Nagaosa, N., Sinova, J., Onoda, S., MacDonald, A. H. & Ong, N. P. Anomalous hall effect. *Rev. Mod. Phys.* **82**, 1539 (2010).
 - 26 Liu, Y., Stavitski, E., Attenkofer, K. & Petrovic, C. Anomalous Hall effect in the van der Waals bonded ferromagnet $\text{Fe}_{3-x}\text{GeTe}_2$. *Phys. Rev. B* **97**, 165415 (2018).
 - 27 Cutler, M. & Mott, N. F. Observation of Anderson localization in an electron gas. *Phys. Rev.* **181**, 1336 (1969).
 - 28 Pu, Y., Chiba, D., Matsukura, F., Ohno, H. & Shi, J. Mott relation for anomalous Hall and Nernst effects in $\text{Ga}_{1-x}\text{Mn}_x\text{As}$ ferromagnetic semiconductors. *Phys. Rev. Lett.* **101**, 117208 (2008).

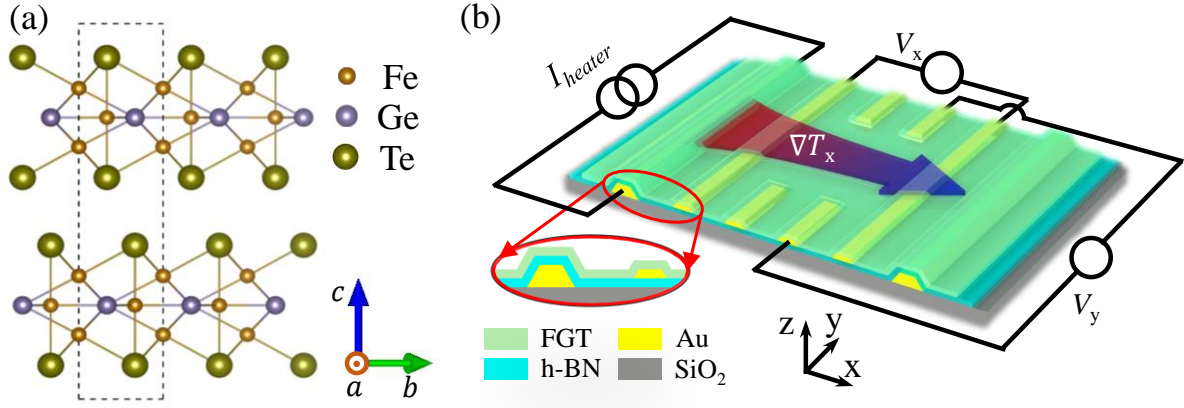


Figure 1. Crystal structure of Fe_3GeTe_2 (FGT) and FGT device for transport measurements. (a) Sideview of Fe_3GeTe_2 crystal structure. Fe_3Ge slabs sandwiched by two layers of Te atoms and a van der Waals gap between the adjacent Te layers. The dashed rectangular box denotes the unit cell. (b) Fe_3GeTe_2 device structure for anomalous Nernst effect. A lateral temperature gradient ∇T_x is applied along x direction, a magnetic field H_z is applied along z direction, both longitudinal and transverse voltages V_x and V_y are measured.

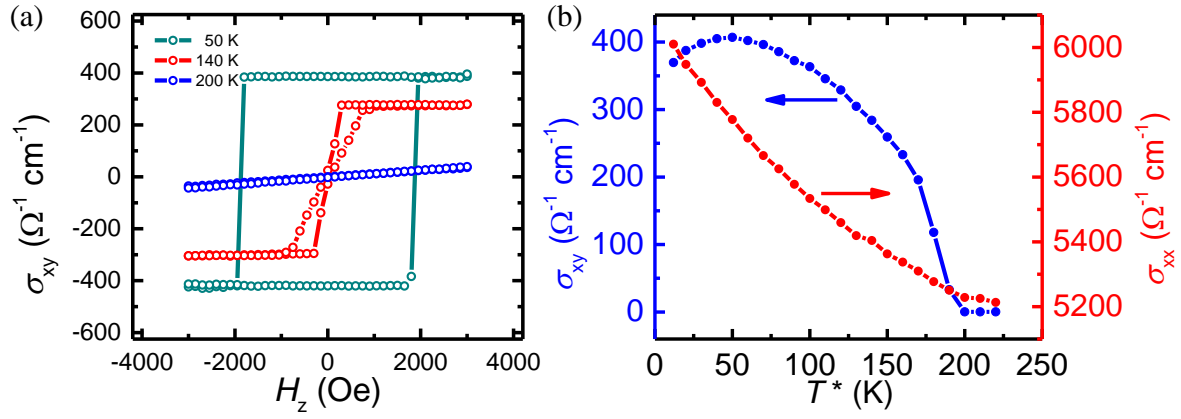


Figure 2. Temperature dependence of anomalous Hall effect (AHE). (a) Hall conductivity σ_{xy} as a function of external applied magnetic field H_z at different temperatures. (b) Temperature dependence of Hall conductivity σ_{xy} (blue curve) extrapolated at zero field and longitudinal conductivity σ_{xx} (red curve). σ_{xy} vanishes around 200 K, the Curie temperature T_c of the sample. The Hall angle $\theta_H = \sigma_{xy}/\sigma_{xx}$ reaches about 0.07 at low temperature.

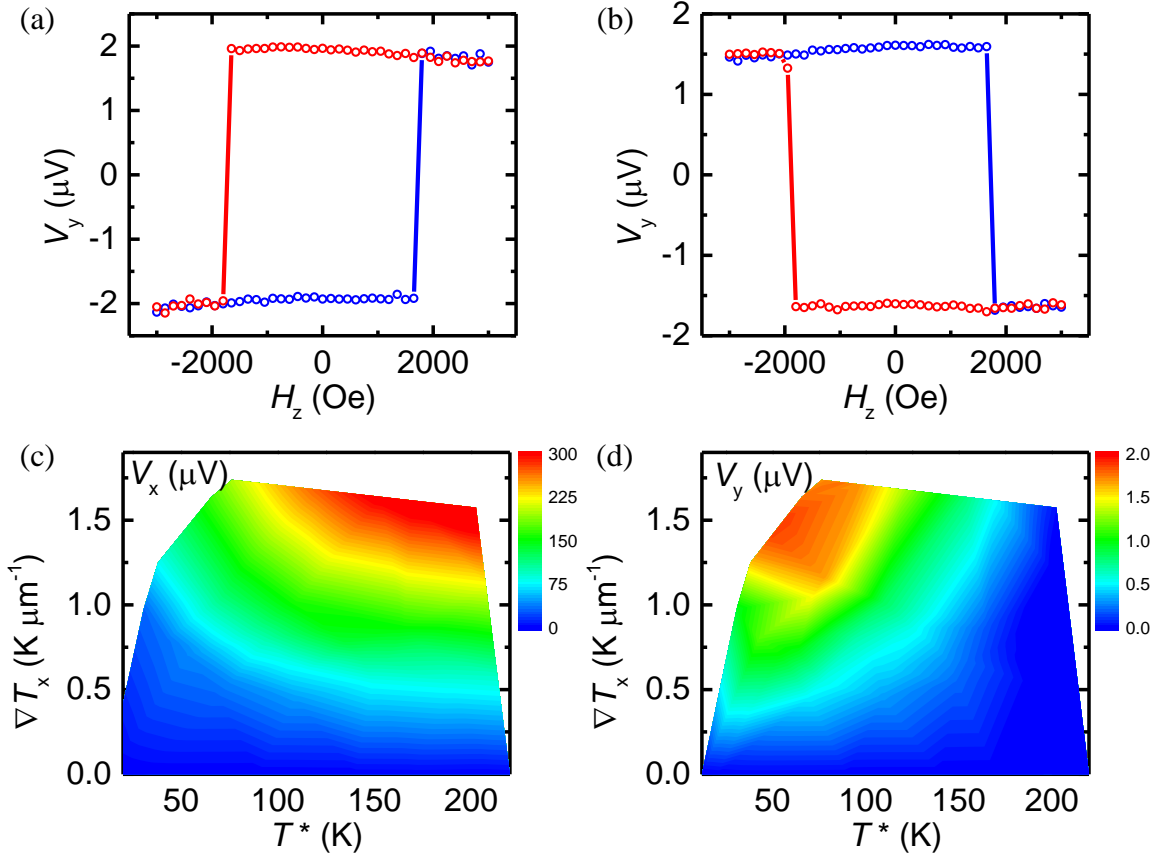


Figure 3. Anomalous Nernst effect (ANE), longitudinal voltage (V_x) and transverse voltage (V_y). (a) Nernst signal V_y as a function of H_z at $\nabla T_x = 1.3 \text{ K } \mu\text{m}^{-1}$. (b) Nernst signal V_y as a function of H_z at $\nabla T_x = -1.1 \text{ K } \mu\text{m}^{-1}$. The data are taken at an effective sample temperature $T^* = 45 \text{ K}$. The blue (red) curve is for increasing (decreasing) magnetic field. (c) Longitudinal voltage V_x (displayed in colors) as a function of temperature and temperature gradient. (d) Transverse voltage V_y (displayed in colors) as a function of temperature and temperature gradient. By definition, $\nabla V_x = -S_{xx}\nabla T_x$ and $\nabla V_y = -S_{yx}\nabla T_x$, both V_x and V_y will increase as a function of ∇T_x . The general trend that V_x (V_y) increases (then decreases) as T^* increases, indicate S_{xx} (S_{yx}) increases (then decreases) with sample temperature T^* .

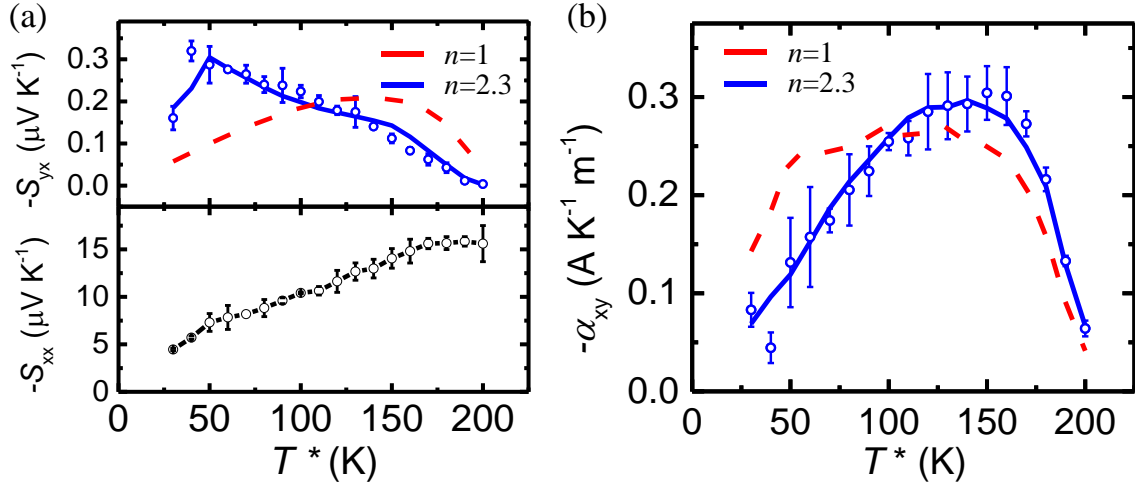


Figure 4. Temperature dependence of S_{yx} , S_{xx} and α_{xy} . (a) Temperature dependence of S_{yx} (top panel) and S_{xx} (bottom panel). S_{xx} and S_{yx} is extracted from the linear fitting V_x and V_y vs ∇T_x respectively. (b) Temperature dependence of α_{xy} . α_{xy} is determined via Eq. (1). Blue solid curve is the best fit using Eq. (2) and (3) for S_{yx} and α_{xy} respectively, and red dashed curve is the best fit with $n=1$.

Supporting Information for

Large anomalous Nernst effect in a van der Waals ferromagnet Fe_3GeTe_2

Jinsong Xu¹, W. Adam Phelan², C.L. Chien¹

¹ Department of Physics and Astronomy, Johns Hopkins University, Baltimore, Maryland 21218, USA

² Department of Chemistry, Johns Hopkins University, Baltimore, Maryland 21218, USA

1. Device fabrication

A dry transfer technique was used to fabricate thin FGT film device for the ANE study. Thin flakes of FGT and h-BN were mechanically exfoliated from their bulk crystals onto Si substrates covered by a 300 nm thermal oxide layer. First, we used standard e-beam lithography with MMA/PMMA bilayer resist to fabricate local heater electrodes. Au electrodes (40 nm) were deposited on Si/SiO₂ (300 nm) empty wafer using an e-beam source and a 5 nm Ti underlayer for adhesion (Fig.S1 (a)). Then a stamp, which consisted of a thin layer of poly(propylene carbonate) (PPC) on polydimethylsiloxane (PDMS) supported by a glass slide, was used to pick up an exfoliated h-BN flake (~20 nm) and transfer onto pre-patterned local heater (Fig.S1 (b)). After that, a second e-beam lithography was used to fabricate contact electrodes. Au electrodes (20 nm) were deposited on Si/SiO₂ (300 nm)/h-BN (20 nm) with a 3 nm Ti underlayer for adhesion (Fig.S1 (c)). Finally, another PPC stamp was used to pick up an exfoliated FGT flake (20~40 nm) and transfer onto the pre-patterned contact electrodes (Fig.S1 (d)).

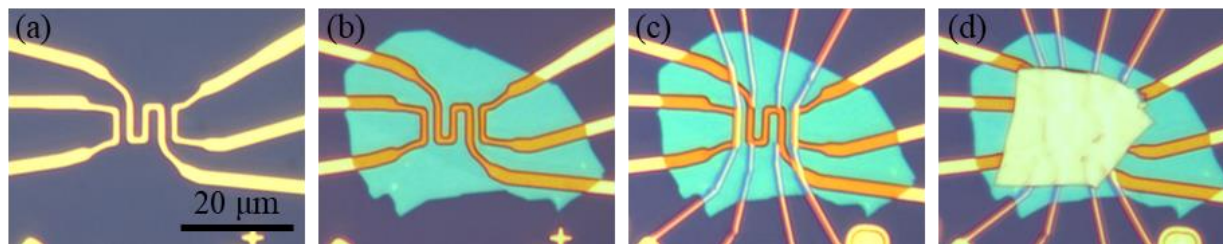


Figure S1. Optical images of FGT devices. (a) Local heaters on Si/SiO₂ substrate. (b) h-BN on top of local heaters. (c) Au electrodes for electrical contact on h-BN. (d) FGT transferred onto prepatterned electrodes. The scale bar is 20 μm.

2. FGT bulk crystal growth

High-quality FGT single crystals were grown by the chemical vapor transport method. High-purity elements were stoichiometrically mixed and sealed under vacuum in a quartz tube with a small quantity of iodine. The tube was placed into a two-zone horizontal furnace with the hot end at 750 °C and the cold end at 650 °C. Shiny plate-like single crystals with typical dimensions of 3 mm × 3 mm × 0.25 mm were then obtained. The high quality of the bulk materials is confirmed by X-ray diffraction (XRD) (Fig.S2) and superconducting quantum interference device (SQUID) (Fig.S3). The c-axis lattice constant extracted from the XRD data in Fig.S2 (a) is 16.36 Å. And the XRD ϕ scan along (016) plane shows six-fold symmetry (Fig.S2 (b)). The magnetization measurement show that the saturation magnetization is about 310 emu cm⁻³ with a magnetic moment of 1.25 μ_B per Fe atom (Fig.S3 (a)), and Curie temperature is about 200 K (Fig.S3 (b)).

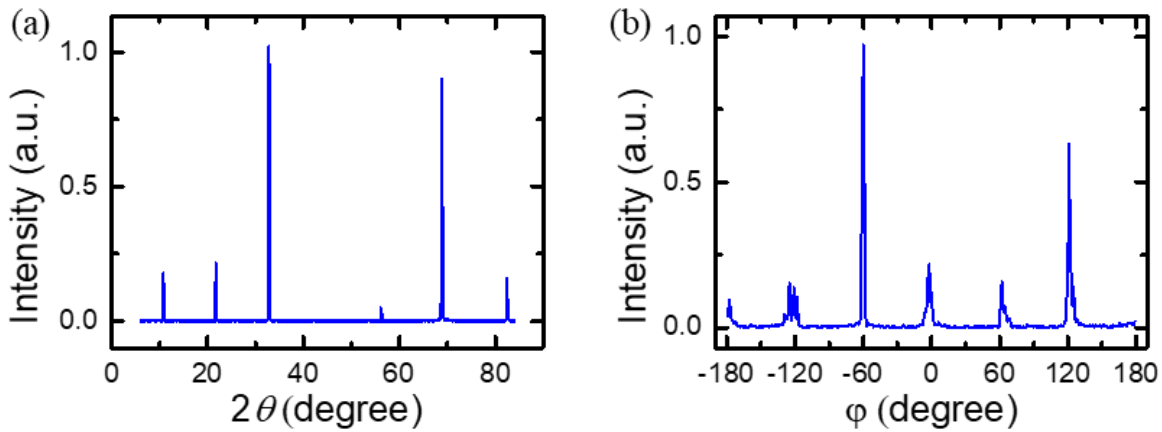


Figure S2. XRD on single crystal FGT. (a) XRD 2θ-ω scan of FGT (001) planes. (b) XRD ϕ scan of FGT (016) plane.

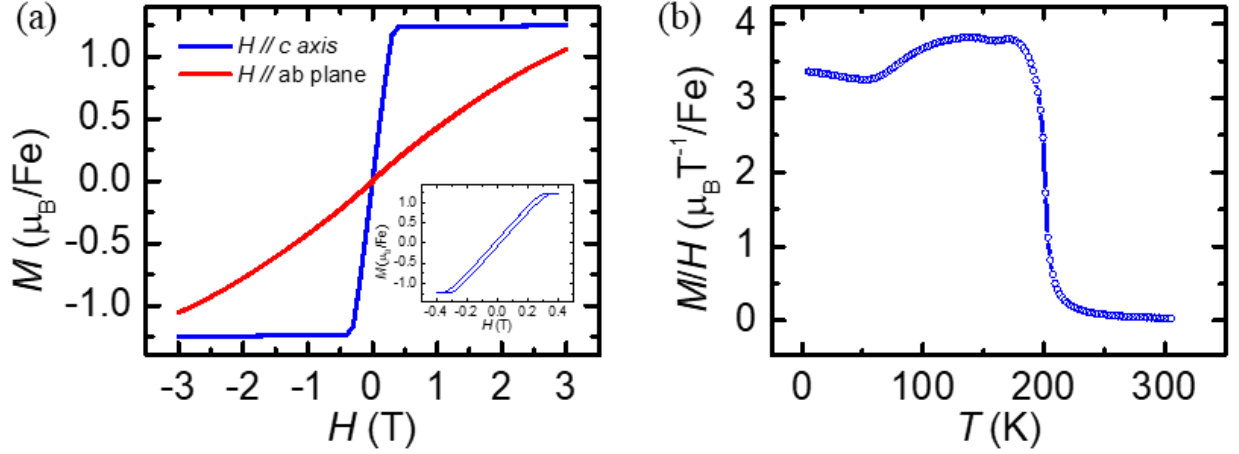


Figure S3. Magnetic properties of single crystal FGT. (a) Magnetization loops of bulk FGT at 5 K. Inset is the zoom-in around 0 field for H applied along c axis. (b) Temperature dependence of the magnetization M divided by applied field H , H is fixed at 100 Oe along c -axis.

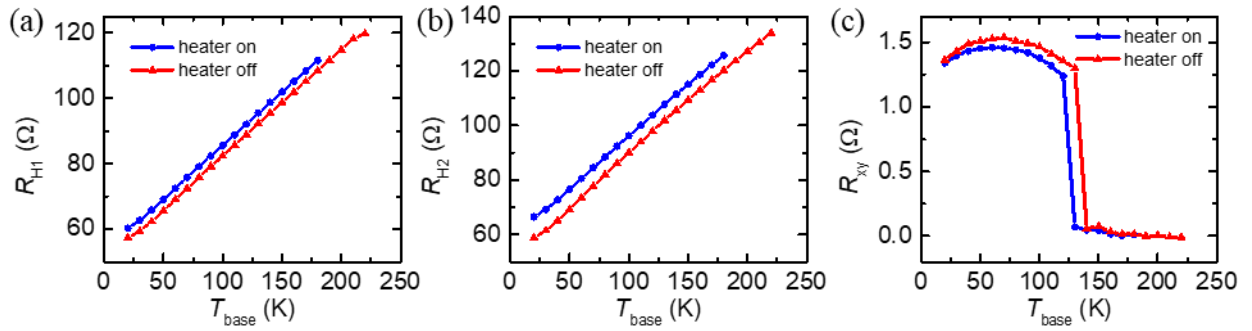


Figure S4. Temperature dependence of heater resistance and AHE. (a) Temperature dependence of heater H1 resistance. (b) Temperature dependence of heater H2 resistance. (c) Temperature dependence of AHE. Blue curves are resistance when heater is off, and red curves are resistance when 10 mA current is applied to heater H2.

3. Temperature calibration

The local temperature of the heater is calibrated by the heater resistance, and the effective sample temperature T^* is calibrated by the AHE signal. T_{base} is the temperature of the cryostat. First, we apply a small current (1 μA) to measure the heater resistance and AHE. In this case, the heating effect is negligible, the temperature of the heater and sample is basically the same to T_{base} . These three temperature dependence of resistance curves (blue curves in Fig.S4) are used as

calibration curves to measure the local temperatures. For example, when 10 mA current is applied to heater H2 (red curves in Fig.S4), local temperature of heater H1 $T_{H1} \approx T_{\text{base}} + 12$ K, $T_{H2} \approx T_{\text{base}} + 20$ K, and $T^* \approx T_{\text{base}} + 14$ K.

4. Nernst signal contribution from vertical temperature gradient ∇T_z

Because the anomalous Nernst signal V is proportional to $\nabla \mathbf{T} \times \mathbf{M}$, a voltage signal along y -axis V_y could be generated by $\nabla T_x \times M_z$ or $\nabla T_z \times M_x$. To eliminate the possible contribution from the vertical temperature gradient ∇T_z , we measure the transverse voltage V_y as a function of external applied magnetic field H_x while keeping the same heater current (14 mA) as used in the main text in Fig. 3a. As seen in Fig. S5, there is no appreciable Nernst signal with fields less than 3000 Oe. Therefore, the Nernst signal in the main text is from lateral temperature gradient ∇T_x .

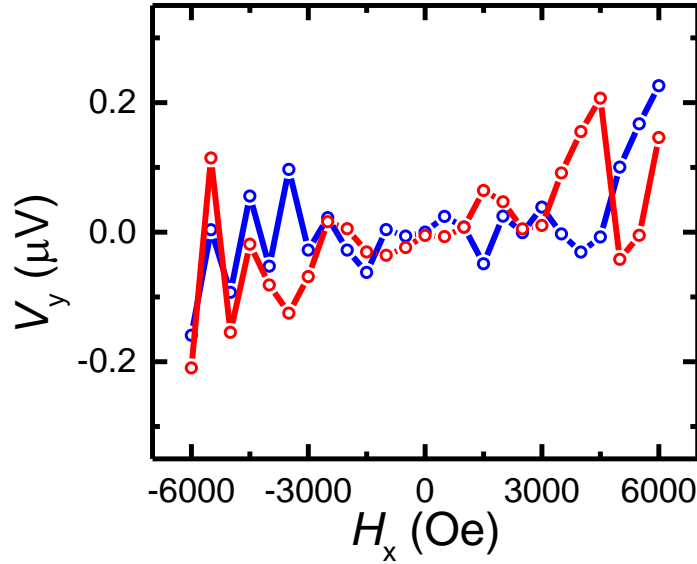


Figure S5. Transverse voltage V_y as a function of external applied magnetic field H_x . The blue (red) curve is for increasing (decreasing) magnetic field.